01 Feb 2023

Rheological Characterization of Ultra-High Performance Concrete for 3d Printing

Arun R. Arunothayan

Behzad Nematollahi

Kamal Khayat
Missouri University of Science and Technology, khayatk@mst.edu

Akilesh Ramesh

et. al. For a complete list of authors, see https://scholarsmine.mst.edu/civarc_enveng_facwork/2247

Recommended Citation

Rheological characterization of ultra-high performance concrete for 3D printing

Arun R. Arunothayan [a,*], Behzad Nematollahi [a,b], Kamal H. Khayat [c], Akilesh Ramesh [a], Jay G. Sanjayan [a]

[a] Center for Smart Infrastructure and Digital Construction, Swinburne University of Technology, Hawthorn, VIC, Australia
[b] Department of Civil and Structural Engineering, The University of Sheffield, Sheffield, United Kingdom
[c] Department of Civil, Architectural and Environmental Engineering, Missouri University of Science and Technology, Rolla, MO, USA

ARTICLE INFO

ABSTRACT

The authors recently developed a 3D-printable ultra-high performance fiber-reinforced concrete (3DP-UHPFRC) for additive construction of structural members with significantly reduced reliance on steel bars. This study investigates the rheological behavior of the developed 3DP-UHPFRC. The effects of two major factors affecting the performance of 3DP-UHPFRC, namely steel fiber volume (0, 1%, and 2%) and nano-clay (NC) content (0, 0.1%, and 0.2% by binder mass) on workability, static yield stress, dynamic yield stress, and apparent viscosity were determined. Test results showed that the inclusion of steel fibers and NC reduced the workability and led to a significant increase in the static yield stress, dynamic yield stress, and apparent viscosity. However, the effect of NC content on the rheological properties became negligible in the mixtures made with 2% fiber content. Similarly, the effect of steel fiber volume became negligible in the mixtures made with 0.2% NC. In addition, the influence of changes in rheology due to the addition of steel fiber and NC on the extrudability and buildability of the mixtures were investigated by 3D-printing of 500 mm high hollow columns with three different print speeds. The results showed all mixtures exhibited satisfactory extrudability (i.e., no blockage of extruder or tearing of filaments was observed). In addition, the buildability of the mixtures increased as the steel fiber and NC contents increased.

1. Introduction

Extrusion-based 3D-concrete-printing (3DCP) is an emerging digital construction technology in which a cementitious material is extruded via a nozzle to build concrete elements layer-by-layer. This technique gives occasion to the construction of complex geometries without the use of expensive formwork, which generally impedes the shape of concrete elements. By eliminating the formwork, this technique can significantly reduce construction waste, while enabling a faster and cheaper construction process. Due to these benefits, the 3DCP technique is of growing interest in both academia and industry [1–3].

The widespread application of the 3DCP technique is currently limited by the practical complications in understanding and characterizing the printable materials in their fresh state [4]. Non-Newtonian fluids, such as concrete, behave as solids under some circumstances and as liquids, otherwise. The solid-like behavior is observed when the applied shear stress is less than the critical yield stress of the material.

On the contrary, the liquid-like behavior is observed when the applied shear stress exceeds the critical yield stress. The resistance to the flow is an inherent characteristic of the material, defined as its viscosity [5]. The ideal 3DCP material should simultaneously have low viscosity (to allow uninterrupted flow during the extrusion) and high yield stress (to retain shape after deposition under the load of subsequent layers printed on top) [6]. Since the yield stress and viscosity of the cementitious materials generally increase with time and the hydration kinetics, these two confronting requirements pose a critical timeframe for printing of the material. Earlier studies explored qualitative 'trial and error' approaches to establish the boundaries of the aforesaid timeframe [7,8]. However, these qualitative measures are printer domain-specific and cannot be universally endorsed. Therefore, further efforts have been made to characterize the fresh properties of the print material in fundamental terms of workability, viscosity, and shear stress [9–14].

Several test methods are proposed to characterize the fresh properties of print materials. Slump tests and flow table tests are standardized

---

* Corresponding author.
E-mail address: rarunothayan@swin.edu.au (A.R. Arunothayan).

and field-oriented protocols to measure the workability of concrete mixtures. Tay et al. [14] defined a framework for an uninterrupted printing process using the slump test and flow table test outcomes. Soltan and Li [12] used the loss of workability with time as an indicator for the structural build-up of the printed structures. To study the viscosity and the yield stress of the fresh mixtures, coaxial rheometers are most widely used. It measures the torque/force exerted on the fresh material at rotational velocities specified by the user as a time function. By converting the rotational velocity and the corresponding torque/-force into shear rate and shear stress, respectively, the flow behavior of the material can be evaluated at different ages. However, the use of coaxial rheometers for high yield stress print materials has been contested over reasons such that the shearing of high yield stress materials disturbs the homogeneity and gives occasion to plug flow [15,16]. In that regard, application-specific approaches such as penetration test [17,18], squeeze flow test [19,20] and direct shear test [9] have been developed for high yield stress print materials. In a latest study, Ivanova et al. [21] concluded that the failure predictions were not accurate in any of these methods, though strong linear correlations were found. The predictions from the coaxial rheometer analyses seemed to slightly underestimate the actual failure of 3DCP materials, which allows for a safety net for design purposes.

In a previous study by the authors, a 3D-printable ultra-high performance fiber-reinforced concrete (3DP-UHPFRC) was developed [22, 23]. The high compressive strength and the ductility of UHPFRC provide a good opportunity to explore the geometrical design freedom that 3DCP has to offer. However, a review of the literature yields contrary observations of the rheological properties of UHPFRC mixtures [15,24–31]. Inconsistent flow characteristics of UHPFRC have been previously reported, owing primarily to the wide range of material selection, which contributes significantly to the performance of UHPFRC [25]. While some studies [25,26] found a linear relationship between the shear stress and shear rate (i.e., constant viscosity) in UHPFRC mixtures, other studies [27–29] showed non-linear flow behavior (i.e., variation in viscosity). Among the studies that observed non-linearity, contradictory shear-thickening and shear-thinning flow models were reported, attributing to the change in dominant forces between the particles at various shear rates [30]. Moreover, flow behavior between UHPFRC paste, mortar, and composite was also inconsistent in the literature [28, 31]. These differences in the flow behavior of UHPFRC mixtures indicate that a distinctive flow characterization is essential for 3DP-UHPFRC mixtures, considering the substantial demands of 3DCP process on the print materials.

The rheological characteristics relevant to 3DCP such as extrudability and buildability of the 3DP-UHPFRC mixtures heavily depend on the selection and use of raw materials. These raw materials in the 3DP-UHPFRC mixtures can be categorized into materials that form the matrix (binder, sand, water, and high-range water-reducing admixture), fibers and viscosity modifiers that facilitate the printability. For consistency with the authors' previous works, the developed 3DP-UHPFRC matrix was not altered in this study. While it is essential to add fibers in UHPFRC mixtures to achieve the required ductility for UHPFRC, addition of high fiber content can lead to clogging and blockages during the extrudability stage, especially when smaller nozzles were employed [32]. Meanwhile, viscosity modifiers such as nano-clay (NC) were used in other studies to improve viscosity, fiber distribution and thixotropic properties of 3D printable mixtures [33,34]. Zhang et al. [33] concluded that the use of NC at 2% mass percentage of binder improved the green strength and buildability of the concrete in addition to thixotropy. However, the excessive use of NC can cause blockages or tearing of filaments and affect extrudability [34]. Additionally, the appropriate NC content needed to facilitate printability depends on the initial rheological properties of the mixtures prior to any addition of NC. Since the existing literature on UHPFRC mixtures (without any NC) yields contrary rheological observations, as discussed earlier, it is essential to characterize the rheology of 3DP-UHPFRC mixtures at varying
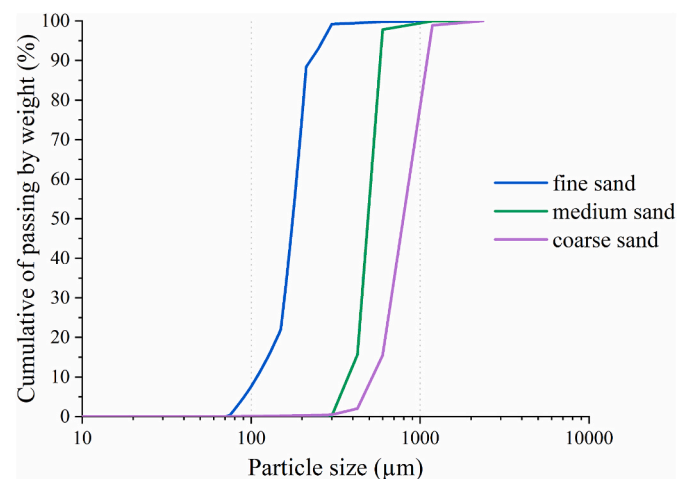

Fig. 1. Particle size distribution of the sands. Reproduced from Ref. [22].

Table 1
Properties of straight micro steel fibers [32,36].

Length (mm)	Diameter (μm)	Elastic modulus (GPa)	Tensile strength (MPa)
6	200	200	2500

concentrations of fibers and NC. In this way, the developed 3DP-UHPFRC composite can be tailored for printing applications efficiently. This was the main motivation for this study.

In this study, the rheology of the 3DP-UHPFRC was characterized by varying steel fiber volume and NC content. The initial workability was measured using the flow table tests. The flow properties (i.e., dynamic yield stress and viscosity) and the static yield stress, which affect the extrudability and buildability of 3DCP, respectively, were measured using a rotational rheometer. The rheological measurements were further supported by 3D printing trials to assess the extrudability and the buildability of the mixtures.

2. Materials and mixture design

The UHPFRC binder contained 70% General Purpose (Type GP) Portland cement and 30% densified silica fume, by mass percentage. Three types of sieve-graded silica sands were used. The fine, medium, and coarse silica sands had median particle sizes (D50) of 176 μm, 498 μm, and 840 μm, respectively. Fig. 1 presents the particle size distributions of the sands [22]. The binder-to-sand-to-water mass ratios were set at 1:1:0.16.

A polycarboxylate ether-based high range water reducing admixture (HRWRA) solution (approximately 35% solids) was used at 1% by mass of binder. Straight micro steel fibers with an aspect ratio of 30 were used at 0, 1%, and 2% volume percentage of the mixture. The micro steel fibers are coated with brass to avoid corrosion. The properties of the micro steel fibers are given in Table 1. These fibers are purpose-cut to be relatively smaller in length (6 mm) than the steel fibers generally used in conventional mold-cast UHPC (up to 25 mm in length) to ease the extrusion process without fiber clogging and simplify the handling of fibers. Nevertheless, it is highly recommended to use personal protective

Table 2
Properties of NC (as reported by the supplier).

pH	Specific gravity (dry powder)	Water solubility (Cl^{-1})	Acid solubility (Cl^{-1})
8.5-9.3	2.29	<001	0.007

Table 3

Chemical composition of NC (as reported by the supplier).

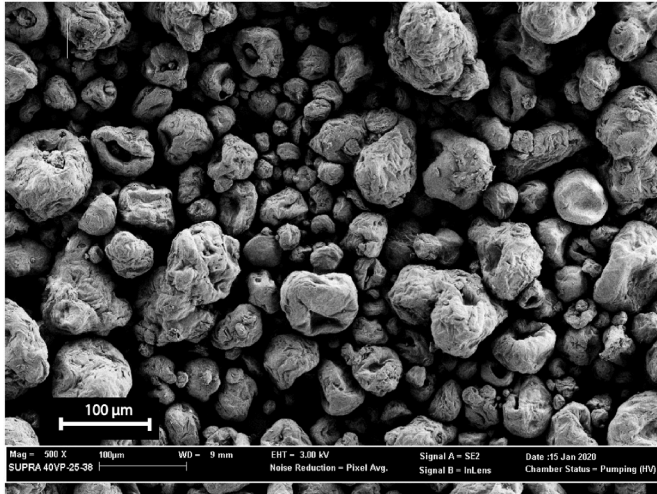| Oxides	Wt. %
SiO_2	55.20
Al_2O_3	12.20
MgO	8.56
Fe_2O_3	4.05
CaO	1.98
K_2O	0.68
P_2O_5	0.65
Na_2O	0.53
Ti_2O	0.49
LOI	15.66

Fig. 2. Scanning electron microscopic image of NC (3D lattice structure).

Table 4

Mixture proportions of investigated mixtures.

Mixture ID	NC[a]	Fiber[b]
NC0–F0	0	0
NC1–F0	0.1	0
NC2–F0	0.2	0
NC0–F1	0	1
NC1–F1	0.1	1
NC2–F1	0.2	1
NC0–F2	0	2
NC1–F2	0.1	2
NC2–F2	0.2	2

[a] By mass percentage of binder.
[b] By volume percentage.

equipment during handling of steel fibers to avoid any potential hazards.

A highly purified hydrous magnesium aluminosilicate NC was used at 0, 0.1%, and 0.2% mass percentage of the total binder. The physical and chemical properties of the NC are given in Table 2. The NC has an average particle length of 1.5–2 μm and an average diameter of 30 nm [35]. In addition, the chemical composition of NC is presented in Table 3. The scanning electron microscopic images of NC are provided in Fig. 2. The development of the 3DP-UHPFRC mixture by achieving the highest particle packing was discussed in detail elsewhere [22].

As shown in Table 4, nine mixtures with different contents of NC and steel fibers were prepared to study the effects of steel fibers and NC on the rheology of the UHPFRC mixtures. The denotations of the mixtures are as follows: NC0F0 –mixture with neither NC nor steel fibers; NC1F2 –mixture with 0.1% NC by mass of binder and 2% fiber volume fraction. In this manner, the rest of the mixture denotations can be inferred.

3. Experimental procedure

3.1. Specimen preparation

The UHPFRC mixtures were prepared using a Hobart mixer of 60-L capacity. The granular ingredients (binder and sand) were initially dry mixed for 3 min at low speed. About 75% of the water was initially added to the dry materials and mixed for 5 min at low speed. The remaining water was mixed with the HRWRA and added in two steps as recommended by Wille et al. [37]. The mixing was continued at low speed until a workable mixture was achieved. Thereafter, the micro steel fibers (if any) were added gradually and mixed for 3 min at low speed followed by 6 min of mixing at high speed. The mixing was briefly paused to visually inspect complete dispersion of the micro steel fibers in the mixture. Finally, the NC was added (if any) and mixed for 3 min at high speed. This mixing protocol was similar to the authors' previous works [22,32].

3.2. Fresh properties

The workability of the fresh mixtures was assessed using the flow table test as per ASTM C1437 [38]. The mean values of the two orthogonal spread diameters were collected before and after 25 drops of the flow table.

The rheological behavior of the mixtures was determined using a Couette-type rotational rheometer (Viskomat XL). A six-blade vane probe, with the diameter and height of each blade being 69 mm, was used to approach the inner cylindrical (coaxial) geometry. A 3.5-L capacity rheometer vessel with a diameter of 135 mm and a height of 170 mm was used as the outer cylinder. The wide gap between the inner and outer cylinders was recommended for the measurements of fresh mixtures with sand and fibers such as UHPFRC [15,39]. At the end of mixing, the fresh mixture was poured into the rheometer vessel and pre-sheared at 60 rpm for 30 s to avoid any initial structural build-up. When the complete breakdown of the test sample was achieved, the applied shear was reduced in a step-by-step process. At each step, the mixture was sheared at a constant shear rate for up to 10 s to establish stress equilibrium (see Fig. 3(a)). The rotational velocity and the corresponding torque were recorded at each stress equilibrium state to analyze the dynamic flow behavior of the mixtures. Once the shear rate was completely removed, the material rest time began. Then, a constant rotational velocity of 0.1 rpm was applied for 20 s after rest times of 5, 10, 15, 20, 30, 45, and 60 min to determine the structural build-up at rest, as shown in Fig. 3(b). The maximum value of the torque (i.e., the torque required to initiate shearing of the mixture) was recorded at each rest time. All measurements were sampled at a rate of 10 s^{-1}. The rotational velocity (N) and the corresponding torque (T) were then translated into shear rate ($\dot{\gamma}$) and shear stress (τ) using Eq. (1) and Eq. (2), respectively [40].

$$\dot{\gamma} = \frac{R_0^{\,2} + R_i^{\,2}}{R_0^{\,2} - R_i^{\,2}} 2\pi N \tag{1}$$

$$\tau = \frac{R_0^{\,2} + R_i^{\,2}}{4\pi h R_0^{\,2} R_i^{\,2}} T \tag{2}$$

where R_0 is the inner radius of the rheometer vessel, R_i is the blade width of the vane probe, and h is the height of the vane probe.

In all trials, single batch mixing approach (i.e., all rest time readings were gathered from the same sample of the mixture) was employed [42]. Generally, measurement errors can occur due to plug flow and fiber migration in high shear materials such as UHPFRC [15]. When the shear rates are lower, the stiff mixture between the rheometer vessel and vane blades may only be sheared partially, which gives occasion for the plug flow. To address this, visual inspection was carried out in all mixtures at the end of the rheological testing. Neither plug cavities nor
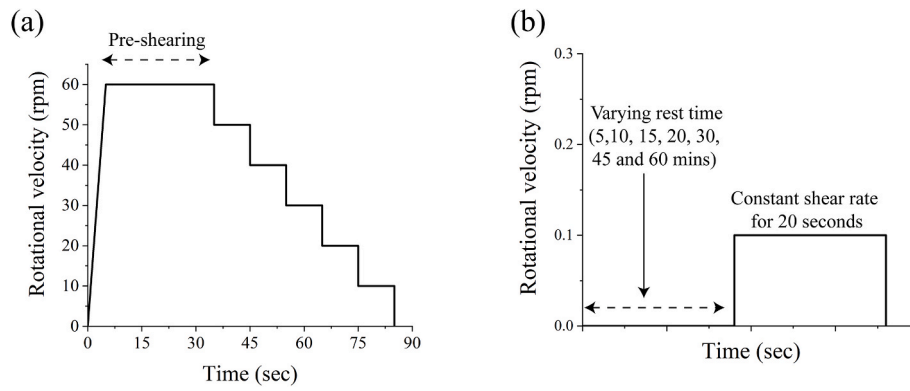
Fig. 3. Applied rotational velocity versus time profiles (a) initial pre-shearing and determination of flow curve in the descending shear rate; and (b) constant shear rate at different rest time intervals to measure static yield stress build-up with rest time. Similar profiles were used in the authors' previous study [41] and elsewhere [34].
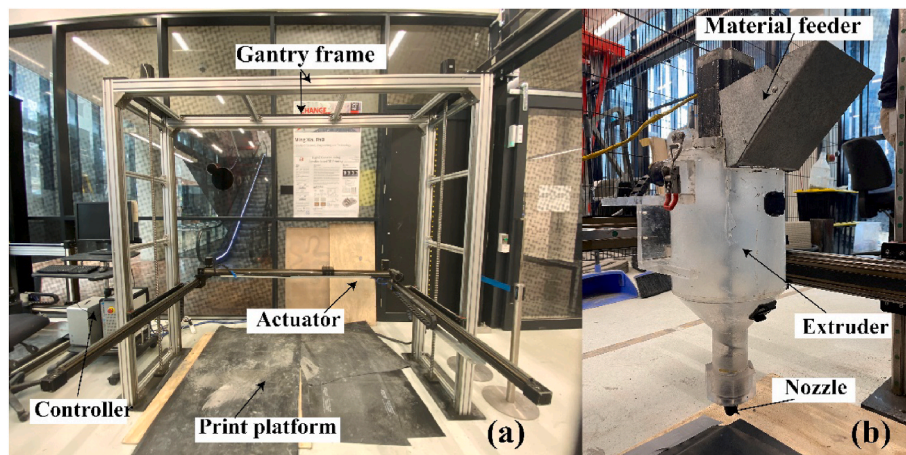

Fig. 4. (a) 3D printer used in the study (b) Extruder and nozzle. Reproduced from [32].

non-homogeneous fiber distributions were observed when the vane was lifted from the vessel. To be extra cautious, three trials of the aforesaid rheological tests were carried out for each mixture to check for any anomalies in data, and the mean values were gathered. On the other hand, when the shear rates are higher, the micro steel fibers may migrate away from the vane blades (i.e., towards the vessel) due to the centrifugal forces arising from the rotational motion; thereby, causing non-homogeneity in the mixtures. Khayat et al. [15] noted that significant particle migration may occur if the thickness of the sheared zone was smaller than or close to the maximum size of the particles in the mixtures. This effect was minimalized in this study by using a large vane size (69 mm) compared to the fiber length (i.e., 6 mm). Additionally, visual inspection at the end of the testing confirmed that there was no segregation of sand particles or fibers in the mixtures.

3.3. Printing trials

A gantry type 3D printer with a print platform volume of 1.8 m × 1.6 m × 1.8 m was employed in this study. An augur-motor system was attached to a cylindrical extruder that was mounted to the lever arm of the printer. The tri-axial Cartesian movement of the lever arm and the rotation of the augur were controlled by a design toolpath generated using G-code. A material feeder was custom-designed and fixed to the extruder inlet to ease uninterrupted supply of fresh material. The extruder outlet was connected to a detachable conical nozzle with 30 mm exit diameter. The printer setup and the extruder are shown in Fig. 4.

To compare the extrudability and buildability of the mixtures with their flow behavior, a printing test protocol was employed to print hollow cylindrical sections. The diameter and the height of the cylindrical sections were 300 mm and 500 mm, respectively. The height of the cylindrical section was made of 50 circular layers, each having a width of 30 mm and a thickness of 10 mm, printed one on the top of another in an uninterrupted print path with no delay time (i.e., the time interval between the printing of end point of a layer and the start point of the adjacent layer was zero). Three different print speeds (30, 50, and 80 mm/s) were employed to study the printing capabilities of the mixtures. Adjusting the print speeds changes the vertical build-up rates, which govern the plastic collapse failure of the hollow cylindrical sections. To maintain the layer width of 30 mm at different print speeds employed, the augur rotational speed was simultaneously adjusted (i.e., higher augur rotational speeds were used at higher print speeds and vice-versa). The 'satisfactory' extrudability and buildability protocols are defined as follows.

- 'Satisfactory' extrudability: Uninterrupted extrusion without any blockage of the extruder, tearing of filaments, bleeding or segregation.
- 'Satisfactory' buildability: No significant vertical distortion, collapse, or onset of flow up to 50-layer height.

The same 'satisfactory' protocols were used by the authors in a previous investigation with reliable outcome measures [41]. Since the printing mechanisms (printer type, extruder and auger setup, print

Table 5
Spread diameters of the mixtures.

Mixture ID	Before[a]	After[b]
NC0–F0	119	151
NC1–F0	120	146
NC2–F0	113	130
NC0–F1	120	144
NC1–F1	116	140
NC2–F1	114	124
NC0–F2	110	127
NC1–F2	105	125
NC2–F2	107	125

Note: All spread diameter values are in mm.
[a] Before drop of the flow table.
[b] After 25 drops of the flow table.

speed, etc …) used in Refs. [32,41] were similar to this study, the same 'satisfactory' protocols, which were representative of these mechanisms, were adopted with rationale. To eliminate any influence of temperature variations, the printing trials were conducted in the same laboratory environment and at the same ambient temperature conditions (i.e., 23 ± 3 °C) as the rheometer tests and the workability tests.

4. Results and discussion

4.1. Workability

The spread diameters of different mixtures are presented in Table 5. The spread values before the drop of the flow table were close to the cone bottom diameter (100 mm), suggesting relatively low slump of the fresh mixtures. After the flow table drop, the spread diameters increased in the range of 124–151 mm. These spread values are quite low

compared to values for the conventionally mold-cast UHPFRC (~300 mm) [37], which indicates the low slump and stiff nature of the printable UHPFRC mixtures. The inclusion of steel fibers and NC hindered the workability. However, the effect of steel fibers was limited in the mixtures having 0.2% of NC (NC2–F1 and NC2–F2 mixtures). Similarly, the effect of NC was minimal in the mixtures made with 2% fiber volume (NC1–F2 and NC2–F2 mixtures).

It must be noted the measuring of workability at different time intervals becomes quite difficult as the spread diameter values of the printable UHPFRC mixtures are very low and closer to the original cone diameter (i.e., 100 mm). Therefore, a more rigorous rheological analysis is needed to characterize the rheological properties of these mixtures.

4.2. Yield stress build-up

According to Roussel et al. [43], the yield stress at a given time t, $\tau_0(t)$, was derived as a function of time, as shown in Eq. (3):

$$\tau_0(t) = \tau_{0,0} + A_{thix}t \tag{3}$$

where $\tau_{0,0}$ is the initial yield stress of the material immediately after pre-shearing (no rest time) and A_{thix} is the linear increment in yield stress with rest time. This model, proposed by Roussel et al. [43], assumes a linear initial hydration rate with rest time. However, this model was later extended by Perrot et al. [19], considering the acceleration in yield stress evolution after the initial hydration period elapsed, extending its validation up to the initial setting of the material. Perrot's model is given in Eq. (4).

$$\tau_0(t) = \tau_{0,0} + A_{thix}t_c\left(e^{\frac{t}{t_c}} - 1\right) \tag{4}$$

where t_c is the characteristic time depending on the curvature of the
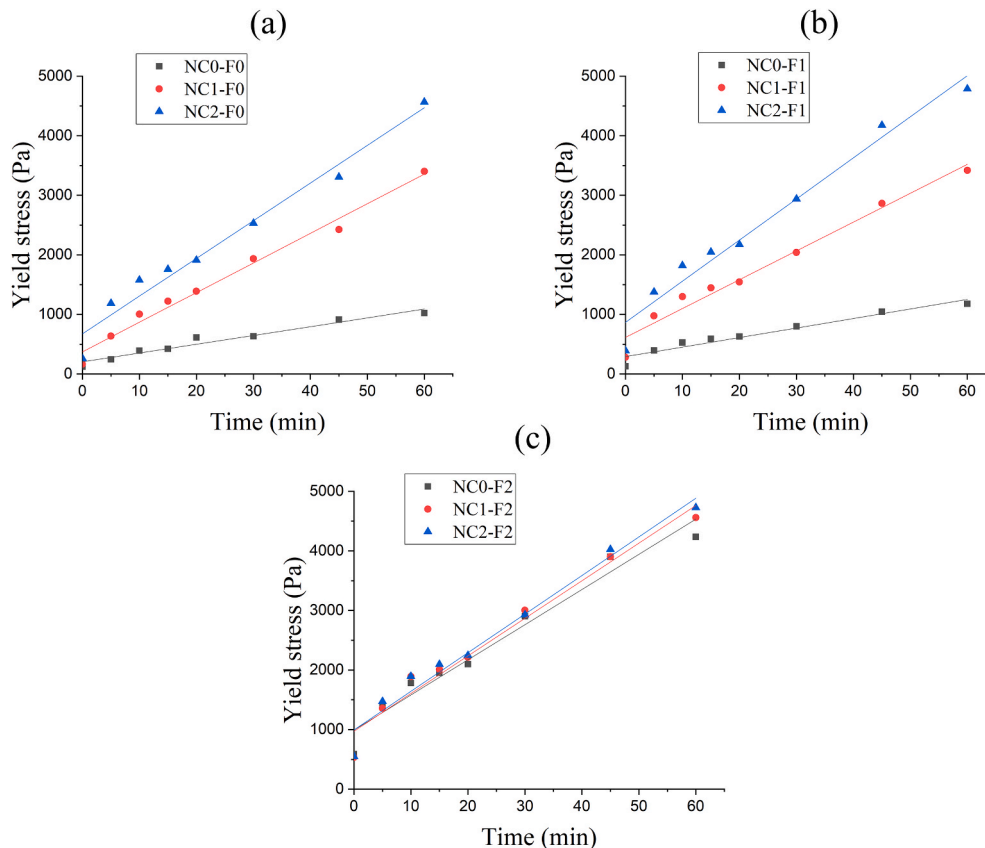

Fig. 5. Variation in yield stress with rest time (a) mixtures without any steel fiber, (b) mixtures with 1% steel fiber, and mixtures (c) with 2% volume steel fiber (note values at zero rest time indicate dynamic yield stress results).

Table 6
Yield stress build-up parameters of the mixtures.

Mixture ID	$\tau_{0,0}$	τ_{floc}	A_{thix}	R^2
NC0–F0	65	180	15	0.950
NC1–F0	205	431	50	0.982
NC2–F0	242	945	63	0.966
NC0–F1	69	326	16	0.937
NC1–F1	290	686	48	0.968
NC2–F1	440	936	69	0.965
NC0–F2	322	1070	59	0.957
NC1–F2	383	973	63	0.966
NC2–F2	467	1006	65	0.969

graph (i.e., the increase in the yield stress evolution rate).

A rapid yield stress increase was observed during the very early age measurements of high yield stress concretes (i.e., up to 5 min of rest time). This was generally attributed to the instant re-flocculation of the wet particles following the removal of pre-shearing torque [10,44,45]. Quantitative evaluation of this very early age rapid flocculation is difficult since frequent application of torque disrupts the sample homogeneity and equilibrium. To address this, non-linear and bilinear models were proposed by Ma et al. [46] and Kruger et al. [45], respectively. Meanwhile, Teng et al. [45] recommended an additional thixotropic stress (τ_{floc}) to adjust for the initial yield stress increase, as in Eq. (5).

$$\tau_0(t > t_r) = \tau_{0,0} + \tau_{floc} + A_{thix}|t - t_r| \tag{5}$$

where t_r is the rest time at the end of rapid flocculation, usually taken as 5 min [44].

The yield stress build-up of the mixtures with rest time is presented in Fig. 5. In all mixtures, the yield stress increased rapidly up to 5 min of rest time, beyond which the increase can be approximated to a linear fit (as per Roussel et al. [43]) up to 60 min. The yield stress values were

curve-fitted to Eq. (5), and the corresponding $\tau_{0,0}$, τ_{floc} and A_{thix} values are presented in Table 6. The acceleration in the yield stress build-up proposed in Eq. (4) was not observed during the test period (i.e., up to 60 min). As such, it can be argued that the $t_c > 60$ min for the mixtures tested in this study. This indicates that the effects of early hydration reactions were not predominant in determining the static yield stress of these mixtures. This observation is consistent with the literature where a dormant hydration period up to several hours was generally observed and attributed to the presence of HRWRA [47,48]. During this dormant period, it is reasonable to assume that the effect of cement hydration is lower than the physical effect of NC. Moreover, Douba and Kawashima [34] attributed the changes in the static yield stresses to the soft colloidal networks between NC and OPC interactions in their recent study. As such, only the physical action of the NC particles was considered in this analysis. The inclusion of NC and steel fibers significantly increased the static yield stresses at all rest times, thereby improving the buildability of the mixtures. The influence of NC on the increase of static yield stresses can be attributed to the formation of lattice microstructure that suspends the solid particles in the fresh mixture, which would in return increase the flocculation rate and static yield stresses [44,49]. However, the effects of NC became insignificant in the mixtures with 2% steel fibers (see τ_{floc} and A_{thix} values in Table 6). It can be hypothesized that the presence of high steel fiber content (as a unidirectional element) in the mixture can physically hinder the formation of NC lattice structure that suspends the solids. On the other hand, the yield stress increment with the steel fiber addition can be explained by the rigidity of the steel fibers, that augments the yield stress of the composite. However, the effects became insignificant in the mixtures having 0.2% of NC (see τ_{floc} and A_{thix} values in Table 6).

Consider a vertical hollow cylindrical section printed at a rate of $H(t)$ using a material with density ρ. The hydrostatic pressure at the bottom layer of the element ($\tau_{hp}(t)$) is given by Eq. (6) [2,19].
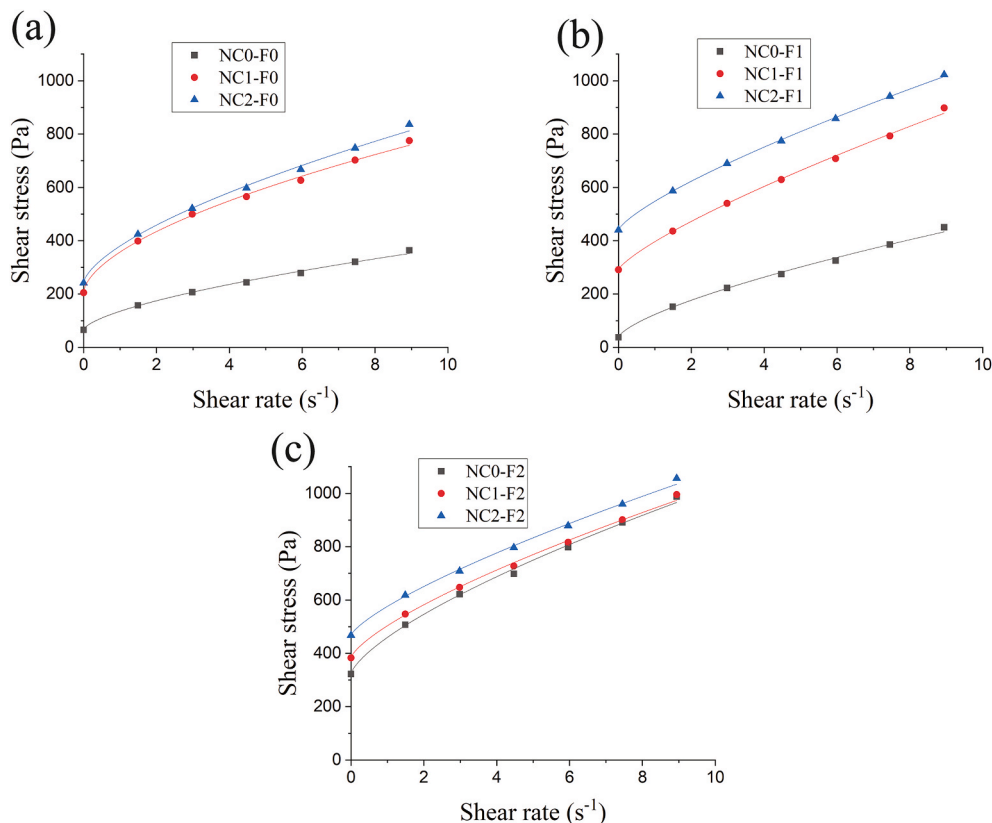

Fig. 6. Flow curves of the mixtures (a) without steel fibers, (b) with 1% steel fibers, and (c) with 2% steel fibers (curve-fitted to Hershel-Buckley model).

Table 7
Hershel Buckley flow parameters of the mixtures.

Mixture	$\tau_{0,H}$	K	n	R^2
NC0–F0	66	70	0.64	0.994
NC1–F0	205	152	0.59	0.995
NC2–F0	242	139	0.65	0.995
NC0–F1	70	60	0.83	0.997
NC1–F1	291	147	0.66	0.995
NC2–F1	440	107	0.77	0.999
NC0–F2	324	130	0.73	0.995
NC2–F1	383	113	0.76	0.997
NC2–F2	468	101	0.80	0.998

Table 8
Modified Bingham flow parameters of the mixtures.

Mixture	$\tau_{0,MB}$	B_1	B_2	R^2
NC0–F0	79	44	−1.5	0.987
NC1–F0	233	94	−3.9	0.983
NC2–F0	267	89	−3	0.988
NC0–F1	53	58	−1.6	0.991
NC1–F1	305	80	−1.7	0.995
NC2–F1	453	83	−2.3	0.997
NC0–F2	344	95	−2.7	0.992
NC1–F2	402	85	−2.2	0.994
NC2–F2	483	79	−1.8	0.995

$$\tau_{hp}(t) = \frac{\rho g H(t)}{\sqrt{3}} \tag{6}$$

The vertical build-up of the cylindrical section can be facilitated only if the material possesses sufficient static yield stress to avoid any collapse during the build-up time (i.e., $\tau_0(t) > \tau_{hp}(t)$). The build-up rate is also influenced by the print speed and the dimensions of the cylindrical section. The higher print speeds reduce the time spent for printing a layer, and therefore increase the build-up rate. Similarly, a cylindrical section with long layer length (i.e., large diameter) will reduce the build-up rate. When the A_{thix} of the print material is high, the print structure can sustain its self-weight (which is controlled by the build-up rate) to facilitate successful printing. If A_{thix} of the print material is low, the vulnerability to plastic collapse failure is high when high print speeds and short layer lengths are employed. Therefore, the selection of print material based on the A_{thix} value is necessary.

As an alternative to Eq. (6), Kruger et al. [45] presented a lower-bound failure model, as in Eq. (7).

$$\tau_{hp}(t) = \frac{\rho g H(t)}{2 F_{AR}} \tag{7}$$

where F_{AR} is a strength-based correction factor based on the layer aspect ratio. F_{AR} is 1 for the aspect ratio of 2 and assumed to be exponentially increasing with lower aspect ratios generally observed in 3D printable mixtures [45,50]. Sanjayan et al. [51] observed F_{AR} to be 1.4 and 2 for non-vibrated and vibrated 3D printable concrete mixtures, respectively. As it can be noted, the predictions from Eq. (6) and Eq. (7) are drastically contradictory based on their initial assumptions. Additionally, it must be noted that the prediction models do not accommodate for elastic buckling or layer pressing effects of the mixtures. Considering these drawbacks, an analytical failure prediction from the printing trials was omitted in the study. However, using Eq. (6) and Eq. (7), the trends of the printing trials and the rheometer analysis can be established to be representative.

4.3. Flow curves and apparent viscosity

In general, 3D printable UHPFRC should exhibit high viscosity and yield stress compared to conventional concrete, therefore power-law model (Hershel-Buckley model), as in Eq. (8), is used to represent its flow curve [5,27].

$$\tau = \tau_{0,H} + K \dot{\gamma}^n \tag{8}$$

where, τ is the applied shear stress, $\tau_{0,H}$ is the Hershel-Buckley yield stress (i.e., the model approximation of $\tau_{0,0}$), $\dot{\gamma}$ is the shear rate, K and n are consistency coefficient and flow index, respectively - two material parameters representing the viscosity of the fresh mixture. The apparent viscosity of the mixture can be determined by $\frac{\tau - \tau_{0,H}}{\dot{\gamma}}$ for any $\dot{\gamma}$.

As an alternative to the Hershel-Buckley model, some literature found the modified Bingham model, as in Eq. (9), to be more representative of the non-linear rheological behavior of cementitious materials [39,52].

$$\tau = \tau_{0,MB} + B_1 \dot{\gamma} + B_2 \dot{\gamma}^2 \tag{9}$$

where, $\tau_{0,MB}$ is the modified Bingham yield stress (i.e., the model approximation of $\tau_{0,0}$), while B_1 and B_2 are dimensionless constants representing the linear term (tangential viscosity at the start of the flow curve) and the second order term of the curves, respectively. In this study, the flow curves of the mixtures were fitted to both models (Hershel-Buckley model and modified Bingham model) to characterize the flow behavior.

Fig. 6 shows the shear stress vs. the shear rate flow curves of the mixtures. These results were curve fitted to the Hershel-Buckley model as in Eq. (8). Table 7 shows the corresponding values of flow parameters (τ_0, K, n) fitted to the model and the coefficient of correlation (R^2) for the sum of least square fitting for each fitting. The values of n are smaller than unity, which indicates that the mixtures can be categorized into pseudo-plastic (i.e., shear thinning) fluids. From Fig. 6 and Table 7, the effect of NC and steel fibers on the flow behavior of the mixtures can be accounted. The addition of NC resulted an increase in the shear stress at all shear rates, regardless of the fiber volume fraction. Similar to the static yield stress discussed earlier, the increase can be attributed to the inherent characteristics of NC to form a lattice microstructure, which supports suspensions of binder and sand particles, which in turn helps particle flocculation [49]. Similarly, the addition of steel fibers resulted an increase in the shear stress at all shear rates, especially when NC is not present in the mixtures. The high rigidity of the steel fibers increases the composite shear stresses to the applied shear rates [53]. These observations are in consistent with the ones discussed in the previous sections.

Alternatively, the experimental data was also curve fitted to the modified Bingham model as in Eq. (9) [39,52]. The corresponding flow parameters ($\tau_{0,MB}, B_1, B_2$) fitted to the modified Bingham model were presented in Table 8. The negative second order B_2 values indicate the shear thinning behavior of the 3DP-UHPFRC mixtures used in the study.

The yield stress values predicted using the modified Bingham model ($\tau_{0,MB}$) is generally higher than those predicted by the Hershel-Buckley model ($\tau_{0,H}$), except for the NC0–F1 mixture. Based on the literature [52], $\tau_{0,MB}$ appeared to be more reliable than $\tau_{0,H}$. Nevertheless, the effects of NC and fibers can be observed on $\tau_{0,MB}$ and $\tau_{0,H}$ in a comparable manner.

As shown in Fig. 7, the apparent viscosity was determined at various shear rates to assess the pseudo-plastic (shear thinning) behavior of the mixtures. In all mixtures, the apparent viscosity decreased as the shear rate increased. As expected, the addition of NC increased the apparent viscosity of the mixtures at all shear rates, indicating the immediate formation and deformation of the lattice structure that suspends the solids temporarily. However, the increment was insignificant in the mixtures made with 2% steel fibers. On the other hand, the addition of steel fibers increased the apparent viscosity due to the presence of adhesive fiber-matrix interface stresses [15]. This behavior coincides with the flow table results given in Table 5.

The Hershel-Buckley parameters derived from Eq. (8) can be used to determine the pumping pressure required to transfer the mixtures for
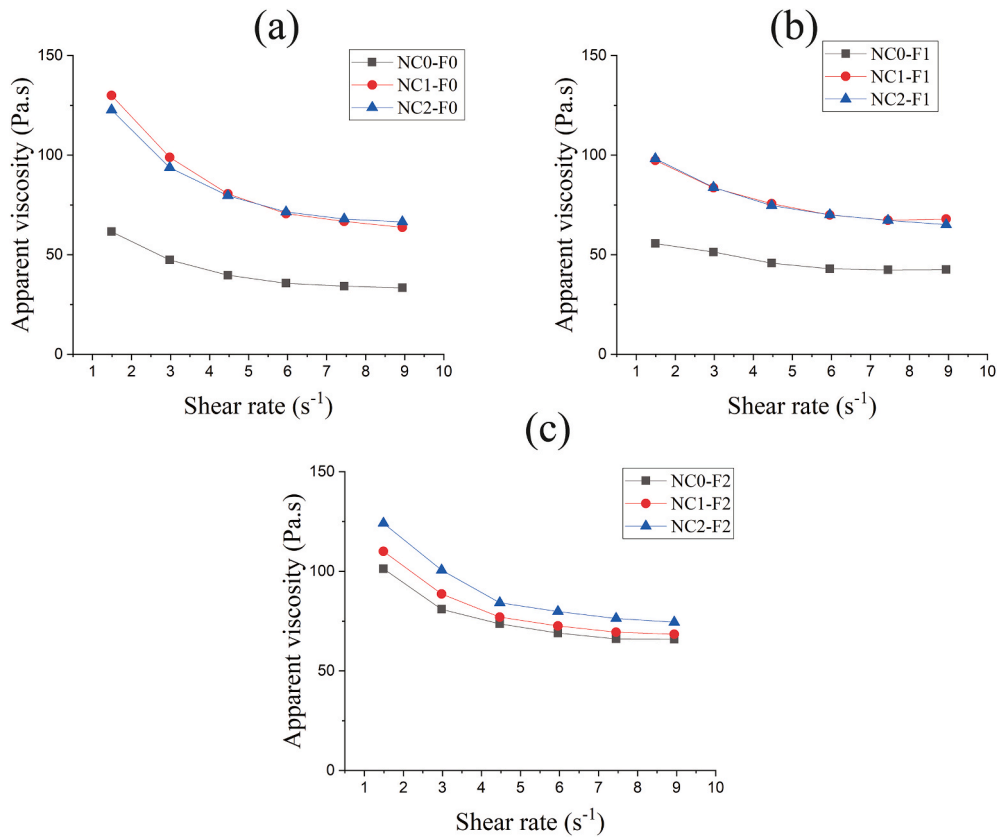
Fig. 7. Apparent viscosity vs. shear rate of the mixtures (a) without steel fibers, (b) with 1% steel fibers, and (c) with 2% steel fibers.

Table 9
Extrudability and buildability trial outcomes.

Mixture	Extrudability			Buildability		
	30 mm/s	50 mm/s	80 mm/s	30 mm/s	50 mm/s	80 mm/s
NC0–F0	Yes	Yes	Yes	No (32)[a]	–	–
NC1–F0	Yes	Yes	Yes	Yes	Yes	No (7)[a]
NC2–F0	Yes	Yes	Yes	Yes	Yes	Yes
NC0–F1	Yes	Yes	Yes	Yes	No (21)[a]	–
NC1–F1	Yes	Yes	Yes	Yes	Yes	No (9)[a]
NC2–F1	Yes	Yes	Yes	Yes	Yes	Yes
NC0–F2	Yes	Yes	Yes	Yes	No (37)[a]	–
NC1–F2	Yes	Yes	Yes	Yes	Yes	No (14)[a]
NC2–F2	Yes	Yes	Yes	Yes	Yes	Yes

[a] The layer number at which the collapse was initially observed was given within the brackets.

printing applications. The pumpability is generally the combination of pump equipment and material characteristics, i.e., the pump type and the corresponding motor mechanism can be selected based on the pumping pressure gradient (P) and volumetric flow rate (Q) of the print material. The relationship between Q and P is complex for Hershel-Buckley fluids. For an uninterrupted laminar flow passing through a circular pipe with a constant radius (R) and constant length (L), the relationship between Q and P can be given as in Eq. (10) [54].

$$Q = \pi \left(\frac{n}{3n+1}\right)\left(\frac{P}{2KL}\right)^{\frac{1}{n}} R^{\frac{3n+1}{n}} \tag{10}$$

Assume the volumetric flow rate is equal to the extrusion rate such that an equilibrium is formed during the printing process. Therefore, the pressure gradients required for the successful pumping can be derived from Eq. (10). For example, the pumping pressure required to pump the

NC2–F2 mixture at a low flow rate of 3.4 l/min via a hose pipe measuring 5 m in length and 25 mm in diameter was calculated to be 144 kPa. This pressure gradient is well within the range of what the commercial concrete pumps can handle (1500 kPa or above).

In addition, from Eq. (10), $P \propto Q^n$. For 3DP-UHPFRC mixtures, exhibiting shear thinning behavior (i.e., $n < 1$ in Table 7), the pressure gradients are less sensitive to the changes in flow rate variations in comparison with a Bingham fluid (i.e., $n = 1$). This suggests the possibility of a plug flow zone forming at the pipe center, resulting in a flatter velocity profile during pumping [15,54].

4.4. Printing trials

Table 9 presents the outcomes of the printing trials of the fresh mixtures at three different print speeds (30, 50, and 80 mm/s). The 'satisfactory' extrudability and buildability outcomes are designated as 'Yes', whereas the unsatisfactory extrudability and buildability are designated as 'No'. The extrusion of all mixtures was successful and uninterrupted at all three print speeds. Higher augur rotational speeds (i.e., higher torque) were employed when NC mass fraction and fiber volume fraction were increased in the mixtures, as to accommodate the higher viscosity and dynamic yield stress of those mixtures. Meanwhile, the buildability of the mixtures was noticeably affected by the print speeds applied. At the print speed of 30 mm/s, all mixtures except the NC0–F0 mixture were deemed 'satisfactory' for buildability. Among those mixtures, the NC0–F1 and NC0–F2 mixtures were deemed 'satisfactory' as the print speed increased to 50 mm/s. The mixtures without NC showed poor buildability as compared to those containing NC. Moreover, when the print speed increased to 80 mm/s, the mixtures with 0.1% NC mass fraction were deemed 'satisfactory', regardless of the fiber volume fraction. Only the three mixtures with 0.2% NC mass fraction (i.e., the NC2–F0, NC2–F1, NC2–F2 mixtures) passed the buildability criteria successfully as the print speed increased to 80 mm/
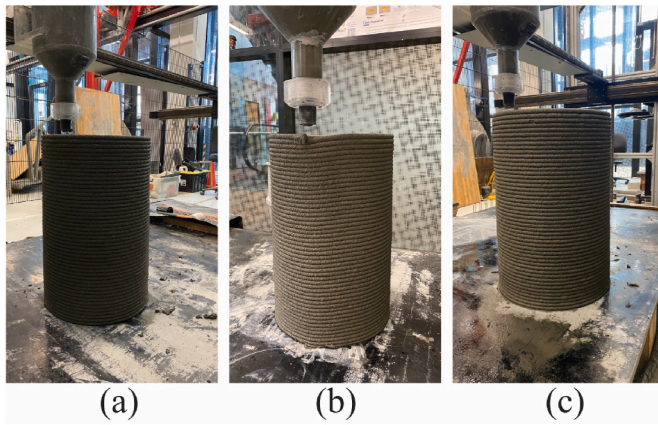
Fig. 8. Hollow cylindrical sections printed at print speed of 80 mm/s (a) NC2–F0 (b) NC2–F1 (c) NC2–F2.

Fig. 9. Snapshot of the plastic collapse failures occurred during the printing trials at print speed of 80 mm/s (a) NC1–F0 (b) NC1–F1 (c) NC1–F2.

s. The layer number, at which the collapse was initially observed, is given within the brackets in Table 9. These observations are in consistent with the measured rheological properties discussed earlier. Since the τ_{floc} and A_{thix} values of the mixtures with 0.2% NC mass fraction are higher, the static yield stress values of these mixtures are higher than the stresses applied on the bottom layers (from the layers deposited above). This reduces the risk of plastic collapse failure. Similarly, τ_{floc} and A_{thix} values of the mixtures without NC are lower, which increases the risk of plastic collapse.

Fig. 8 presents the printed hollow cylindrical sections of the NC2–F0, NC2–F1 and NC2–F2 mixtures that successfully passed the buildability trial at print speed of 80 mm/s. Fig. 9 presents the plastic collapses of the of the NC1–F0, NC1–F1 and NC1–F2 mixtures at print speed of 80 mm/s, which were observed during 7th, 9th, and 14th layers, respectively. The minor increase in the number of layers at the time of collapse indicates the improved buildability with the addition of steel fibers in these mixtures. The deformation of the bottom layers because of the self-weight of the upper layers can be observed from the plastic collapses in Fig. 9, as suggested in the literature [6,55].

5. Conclusions

This study characterized the rheological behavior of a 3D-printable UHPFRC by varying two major contributing ingredients, namely steel fiber content (0, 1% and 2% by volume) and nano-clay contents (0, 0.1% and 0.2% by mass of binder). The following conclusions are drawn:

(a) The workability of the investigated mixtures for 3DCP applications was lower than that of typical UHPFRC mixtures used for casting applications. The addition of steel fibers and nano-clay

further reduced the workability. However, the reducing effect of steel fibers became minimal in the mixtures prepared with 0.2% nano-clay. Similarly, the effect of nano-clay became minimal in the mixtures having 2% steel fibers.

(b) A rapid increase in the static yield stress was observed at 5 min of rest time. Thereafter, the rate of the structural build-up at rest was linear for up to 60 min of rest time. The addition of nano-clay and steel fibers increased the static yield stress of the mixtures at all rest times.

(c) The pseudo-plastic flow behavior of all mixtures followed the power-law model (or Hershel-Buckley model). The apparent viscosity values of the mixtures decreased with shear rate, indicating shear-thinning characteristics. The addition of nano-clay and steel fibers increased the dynamic yield stress, apparent viscosity, and the shear-thinning characteristics of the mixtures.

(d) The extrusion of all mixtures was successful at three different print speeds (30 mm/s, 50 mm/s and 80 mm/s) and no blockage or tearing of filaments was observed. Higher torque was applied to extrude the mixtures when NC and fiber contents were increased.

(e) The buildability of the mixtures was noticeably affected by the print speeds applied in the study. The mixtures without NC showed poor buildability compared to those containing NC. Only the mixtures with 0.2% NC mass fraction passed the buildability criteria successfully at all three print speeds. The printing trial outcomes can be explained using the measured rheological properties of the mixtures.

Declaration of competing interest

The authors declare that they have no known competing financial interests or personal relationships that could have appeared to influence the work reported in this paper.

Data availability

Data will be made available on request.

Acknowledgements

References

[1] J.G. Sanjayan, A. Nazari, B. Nematollahi, 3D Concrete Printing Technology: Construction and Building Applications, Butterworth-Heinemann, 2019.
[2] T. Wangler, N. Roussel, F.P. Bos, T.A. Salet, R.J. Flatt, Digital concrete: a review, Cement Concr. Res. 123 (2019), 105780.
[3] R.A. Buswell, W.L. de Silva, S. Jones, J. Dirrenberger, 3D printing using concrete extrusion: a roadmap for research, Cement Concr. Res. 112 (2018) 37–49.
[4] N. Roussel, Rheological requirements for printable concretes, Cement Concr. Res. 112 (2018) 76–85.
[5] N. Roussel, Understanding the Rheology of Concrete, Elsevier, 2011.
[6] R. Jayathilakage, P. Rajeev, J. Sanjayan, Yield stress criteria to assess the buildability of 3D concrete printing, Construct. Build. Mater. 240 (2020), 117989.
[7] T.T. Le, S.A. Austin, S. Lim, R.A. Buswell, A.G. Gibb, T. Thorpe, Mix design and fresh properties for high-performance printing concrete, Mater. Struct. 45 (8) (2012) 1221–1232.
[8] B. Nematollahi, P. Vijay, J. Sanjayan, A. Nazari, M. Xia, V.N. Nerella, V. Mechtcherine, Effect of polypropylene fibre addition on properties of geopolymers made by 3D printing for digital construction, Materials 11 (12) (2018) 2352.
[9] R. Jayathilakage, J. Sanjayan, P. Rajeev, Direct shear test for the assessment of rheological parameters of concrete for 3D printing applications, Mater. Struct. 52 (1) (2019) 12.

[10] J. Kruger, S. Zeranka, G. van Zijl, An ab initio approach for thixotropy characterisation of (nanoparticle-infused) 3D printable concrete, Construct. Build. Mater. 224 (2019) 372–386.

[11] B. Panda, C. Unluer, M.J. Tan, Extrusion and rheology characterization of geopolymer nanocomposites used in 3D printing, Compos. B Eng. 176 (2019), 107290.

[12] D.G. Soltan, V.C. Li, A self-reinforced cementitious composite for building-scale 3D printing, Cem. Concr. Compos. 90 (2018) 1–13.

[13] D. Lootens, P. Jousset, L. Martinie, N. Roussel, R. Flatt, Yield stress during setting of cement pastes from penetration tests, Cement Concr. Res. 39 (5) (2009) 401–408.

[14] Y.W.D. Tay, Y. Qian, M.J. Tan, Printability region for 3D concrete printing using slump and slump flow test, Compos. B Eng. 174 (2019), 106968.

[15] K.H. Khayat, W. Meng, K. Vallurupalli, L. Teng, Rheological properties of ultra-high-performance concrete-An overview, Cement Concr. Res. 124 (2019), 105828.

[16] S. Muthukrishnan, S. Ramakrishnan, J. Sanjayan, Effect of alkali reactions on the rheology of one-part 3D printable geopolymer concrete, Cem. Concr. Compos. 116 (2021), 103899.

[17] L. Reiter, T. Wangler, N. Roussel, R.J. Flatt, The role of early age structural build-up in digital fabrication with concrete, Cement Concr. Res. 112 (2018) 86–95.

[18] A. Szabo, L. Reiter, E. Lloret-Fritschi, T. Wangler, F. Gramazio, M. Kohler, R. J. Flatt, ACDC: the admixture controlled digital casting and its application to thin folded concrete structures, in: RILEM International Conference on Concrete and Digital Fabrication, Springer, 2020, pp. 956–966.

[19] A. Perrot, T. Lecompte, P. Estellé, S. Amziane, Structural build-up of rigid fiber reinforced cement-based materials, Mater. Struct. 46 (2013) 1561–1568.

[20] R. Wolfs, F. Bos, T. Salet, Early age mechanical behaviour of 3D printed concrete: numerical modelling and experimental testing, Cement Concr. Res. 106 (2018) 103–116.

[21] I. Ivanova, E. Ivaniuk, S. Bisetti, V.N. Nerella, V. Mechtcherine, Comparison between methods for indirect assessment of buildability in fresh 3D printed mortar and concrete, Cement Concr. Res. 156 (2022), 106764.

[22] A.R. Arunothayan, B. Nematollahi, R. Ranade, S.H. Bong, J. Sanjayan, Development of 3D-printable ultra-high performance fiber-reinforced concrete for digital construction, Construct. Build. Mater. 257 (2020), 119546.

[23] R. Arunothayan, B. Nematollahi, S.H. Bong, R. Ranade, J. Sanjayan, Hardened properties of 3D printable ultra-high performance fiber-reinforced concrete for digital construction applications, Rheology and Processing of Construction Materials (2019) 355–362.

[24] M. Zhou, Z. Wu, X. Ouyang, X. Hu, C. Shi, Mixture design methods for ultra-high-performance concrete-a review, Cem. Concr. Compos. 124 (2021), 104242.

[25] A. Arora, M. Aguayo, H. Hansen, C. Castro, E. Federspiel, B. Mobasher, N. Neithalath, Microstructural packing-and rheology-based binder selection and characterization for Ultra-high Performance Concrete (UHPC), Cement Concr. Res. 103 (2018) 179–190.

[26] W. Meng, K.H. Khayat, Improving flexural performance of ultra-high-performance concrete by rheology control of suspending mortar, Compos. B Eng. 117 (2017) 26–34.

[27] J. Dils, V. Boel, G. De Schutter, Influence of cement type and mixing pressure on air content, rheology and mechanical properties of UHPC, Construct. Build. Mater. 41 (2013) 455–463.

[28] A. Yahia, K. Khayat, Applicability of rheological models to high-performance grouts containing supplementary cementitious materials and viscosity enhancing admixture, Mater. Struct. 36 (6) (2003) 402–412.

[29] A. Yahia, Shear-thickening behavior of high-performance cement grouts-Influencing mix-design parameters, Cement Concr. Res. 41 (3) (2011) 230–235.

[30] D. Feys, R. Verhoeven, G. De Schutter, Why is fresh self-compacting concrete shear thickening? Cement Concr. Res. 39 (6) (2009) 510–523.

[31] L. Martinie, P. Rossi, N. Roussel, Rheology of fiber reinforced cementitious materials: classification and prediction, Cement Concr. Res. 40 (2) (2010) 226–234.

[32] A.R. Arunothayan, B. Nematollahi, R. Ranade, S.H. Bong, J.G. Sanjayan, K. H. Khayat, Fiber orientation effects on ultra-high performance concrete formed by 3D printing, Cement Concr. Res. 143 (2021), 106384.

[33] Y. Zhang, Y. Zhang, G. Liu, Y. Yang, M. Wu, B. Pang, Fresh properties of a novel 3D printing concrete ink, Construct. Build. Mater. 174 (2018) 263–271.

[34] A. Douba, S. Kawashima, Use of nanoclays and methylcellulose to tailor rheology for three-dimensional concrete printing, ACI Mater. J. 118 (6) (2021) 275–289.

[35] Acti-Gel Purified Magnesium Aluminoslicate product. https://activeminerals.com/products/acti-gel-208/, 2022. (Accessed September 2022).

[36] A.R. Arunothayan, B. Nematollahi, J. Sanjayan, R. Ranade, S.H. Bong, K. Khayat, Quantitative evaluation of orientation of steel fibers in 3D-printed ultra-high performance concrete, in: RILEM International Conference on Concrete and Digital Fabrication, Springer, 2020, pp. 389–397.

[37] K. Wille, A.E. Naaman, G.J. Parra-Montesinos, Ultra-high performance concrete with compressive strength exceeding 150 MPa (22 ksi): a simpler way, ACI Mater. J. 108 (1) (2011).

[38] ASTM C1437, Standard Test Method for Flow of Hydraulic Cement Mortar, 2007.

[39] D. Feys, J.E. Wallevik, A. Yahia, K.H. Khayat, O.H. Wallevik, Extension of the Reiner-Riwlin equation to determine modified Bingham parameters measured in coaxial cylinders rheometers, Mater. Struct. 46 (1–2) (2013) 289–311.

[40] G. Heirman, L. Vandewalle, D. Van Gemert, O. Wallevik, Integration approach of the Couette inverse problem of powder type self-compacting concrete in a wide-gap concentric cylinder rheometer, J. Non-Newton. Fluid. 150 (2008) 93–103.

[41] A.R. Arunothayan, B. Nematollahi, R. Ranade, K.H. Khayat, J.G. Sanjayan, Digital fabrication of eco-friendly ultra-high performance fiber-reinforced concrete, Cem. Concr. Compos. 125 (2022), 104281.

[42] I. Ivanova, V. Mechtcherine, Evaluation of Structural Build-Up Rate of Cementitious Materials by Means of Constant Shear Rate Test: Parameter Study, Rheology and Processing of Construction Materials, Springer, 2019, pp. 209–218.

[43] N. Roussel, G. Ovarlez, S. Garrault, C. Brumaud, The origins of thixotropy of fresh cement pastes, Cement Concr. Res. 42 (2012) 148–157.

[44] L. Teng, J. Zhu, K.H. Khayat, J. Liu, Effect of welan gum and nanoclay on thixotropy of UHPC, Cement Concr. Res. 138 (2020), 106238.

[45] J. Kruger, S. Zeranka, G. van Zijl, 3D concrete printing: a lower bound analytical model for buildability performance quantification, Autom. ConStruct. 106 (2019), 102904.

[46] S. Ma, Y. Qian, S. Kawashima, Experimental and modeling study on the non-linear structural build-up of fresh cement pastes incorporating viscosity modifying admixtures, Cement Concr. Res. 108 (2018) 1–9.

[47] V. Morin, F. Cohen-Tenoudji, A. Feylessoufi, P. Richard, Evolution of the capillary network in a reactive powder concrete during hydration process, Cement Concr. Res. 32 (12) (2002) 1907–1914.

[48] A. Korpa, T. Kowald, R. Trettin, Phase development in normal and ultra high performance cementitious systems by quantitative X-ray analysis and thermoanalytical methods, Cement Concr. Res. 39 (2) (2009) 69–76.

[49] R. Rafiee, R. Shahzadi, Mechanical properties of nanoclay and nanoclay reinforced polymers: a review, Polym. Compos. 40 (2) (2019) 431–445.

[50] S. Muthukrishnan, S. Ramakrishnan, J. Sanjayan, Technologies for improving buildability in 3D concrete printing, Cem. Concr. Compos. 122 (2021), 104144.

[51] J.G. Sanjayan, R. Jayathilakage, P. Rajeev, Vibration induced active rheology control for 3D concrete printing, Cement Concr. Res. 140 (2021), 106293.

[52] O. H Wallevik, D. Feys, J.E. Wallevik, K.H. Khayat, Avoiding inaccurate interpretations of rheological measurements for cement-based materials, Cement Concr. Res. 78 (2015) 100–109.

[53] B. Zhou, Y. Uchida, Influence of flowability, casting time and formwork geometry on fiber orientation and mechanical properties of UHPFRC, Cement Concr. Res. 95 (2017) 164–177.

[54] P.R. Chhabra, J.F. Richardson, Non-Newtonian Flow and Applied Rheology: Engineering Applications, Butterworth-Heinemann, 2001.

[55] J. Kruger, S. Cho, S. Zeranka, C. Viljoen, G. van Zijl, 3D concrete printer parameter optimisation for high rate digital construction avoiding plastic collapse, Compos. B Eng. 183 (2020), 107660.